



This is the accepted manuscript made available via CHORUS, the article has been published as:

Measurement by antilocalization of interactions between InAs surface electrons and magnetic surface species

Yao Zhang, R. L. Kallaher, V. Soghomonian, and J. J. Heremans

Phys. Rev. B **87**, 054430 — Published 25 February 2013

DOI: [10.1103/PhysRevB.87.054430](https://doi.org/10.1103/PhysRevB.87.054430)

Measurement by antilocalization of interactions between InAs surface electrons and local moments

Yao Zhang,¹ R. L. Kallaher,¹ V. Soghomonian,¹ and J. J. Heremans^{1,*}

¹*Department of Physics, Virginia Tech, Blacksburg, Virginia 24061, USA*

We show that antilocalization measurements can be used to experimentally study the interactions between InAs surface electrons and local moments of the rare earth ions Sm^{3+} , Gd^{3+} and Ho^{3+} on the surface. Magnetic spin-flip scattering and spin-orbit scattering of the accumulation layer electrons are affected by the proximity of the rare earth ions. The spin-flip rate carries information about magnetic interactions. Within the temperature range studied, Sm^{3+} and Gd^{3+} yield temperature-independent electron spin-flip rates in proportion to their magnetic moments. In proximity to Ho^{3+} the InAs electrons however show a spin-flip rate increasing with temperature. We interpret the spin-flip rate due to Ho^{3+} as resulting from transitions between closely spaced energy levels of the ion on the surface. The experiments also show that the strength of spin-orbit interaction can be modified by the surface species.

PACS numbers: 72.15.Rn, 73.61.Ey, 72.15.Qm, 73.25.+i

The spin-exchange interactions between carriers and local moments lead to modified magnetic and transport properties of fundamental and applied interest, and as such form one of the key parameters in spin physics and spin-based technologies. In particular, controllable surface magnetism and its interaction with itinerant electrons in a non-magnetic host has formed the subject of continuous investigations¹⁻⁴. In a series of comparative experiments, we study the interactions which electrons in the accumulation layer formed on the InAs surface experience from local spin moments due to rare earth (RE) ions located on the surface, upon deposition of an aqueous RE nitrate solution. We find that the presence of the RE ions modifies the spin-orbit interaction (SOI) properties and the spin-flip scattering rate of the InAs surface electrons, thus creating a tunable artificial structure where interactions between electrons and local moments, and surface magnetism, determine spin properties and can be studied. The quantum phase coherence properties of the surface electrons form a very sensitive probe both of their quantum states and of the presence of magnetic impurities, exceeding in the latter the sensitivity obtained by direct magnetic measurement^{5,6}. To study the interactions we hence use the weak-localization quantum coherence corrections to the conductivity, caused by interference between backscattered time-reversed electron trajectories. The interference leads to a resistance R with a specific dependence on the magnetic field B applied normally to the surface, under strong SOI known as antilocalization (AL)⁷⁻⁹.

Four characteristic scattering times^{10,11} determine the quantum corrections to the conductivity arising from AL: the elastic scattering time τ_0 as deduced from carrier density and mobility; the SOI scattering time τ_{SO} ; the inelastic scattering time τ_i ; and the magnetic spin-flip scattering time τ_s , which in combination with τ_i determines the electron dephasing time τ_φ . Of particular interest in the present work are the spin-flip time τ_s , carrying the information about the interactions between surface local moments and electrons, and the SOI scattering time τ_{SO} , carrying information about the strength of the SOI. To extract values for τ_s it is advantageous to use a system with pre-existing prominent SOI because the characteristic magnetoresistance of AL shows a turnaround from positive to negative magnetoresistance under increasing B , fa-

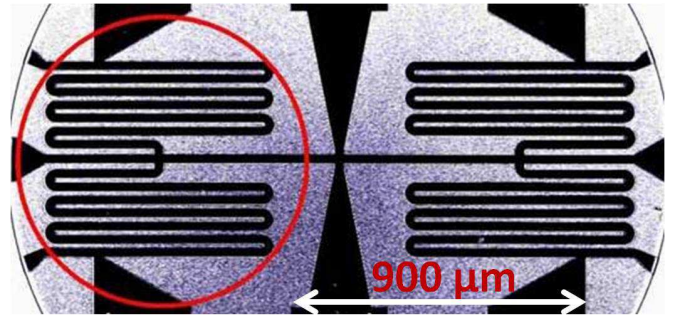


FIG. 1: Optical micrograph of a sample, with twin serpentine InAs mesas (dark areas; light areas are etched to the GaAs substrate).

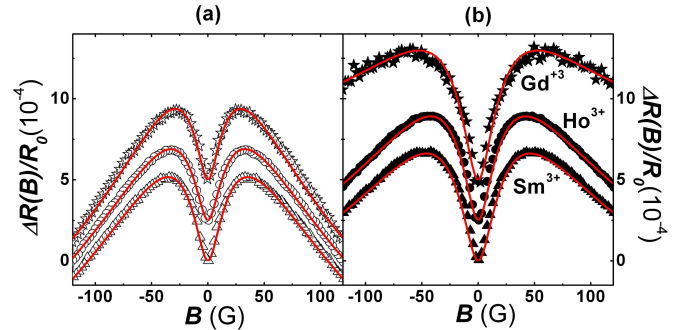


FIG. 2: (a) Magnetoresistance due to AL at 0.4 K on the bare mesas twinned with the Sm^{3+} (triangles)-, Gd^{3+} (stars)- and Ho^{3+} (circles)-covered mesas in (b). (b) Magnetoresistance due to AL at 0.4 K on the covered mesas twinned with the bare mesas in (a) (1 out of 6 experimental points are plotted, curves offset by 2.5×10^{-4}). Solid lines are theoretical fits.

ilitating unique numerical fits of the AL model to the data. It is well established that at the surfaces of InAs the Fermi level E_F is pinned above the conduction band, forming a surface electron accumulation layer and hence a two-dimensional electron system (2DES) at the surface¹²⁻¹⁵. Our experiments require electrons in close proximity to the local moments, satisfied by the InAs surface 2DES. The InAs surface 2DES also has substantial Rashba SOI¹⁶.

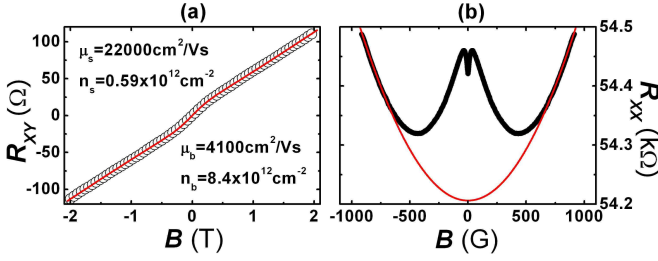


FIG. 3: (a) R_{xy} and (b) R_{xx} data of a bare InAs accumulation layer at 0.4 K. The circles (a) and the bold line (b) are experimental values (in (a) 1 out of 60 experimental points only are plotted). Fine color lines are fitted curves from the two-carrier analysis, which in (b) leads to a parabolic background in R_{xx} .

As shown in Fig. 1, each sample consists of two immediately neighboring twin serpentine mesas. The serpentine increase the observed signal by increasing the channel length to width ratio, and were transferred to 3.75 μm thick n -InAs films, grown on GaAs (001) substrates through metal organic chemical vapor deposition. For each sample, onto only one of the twin mesas 0.01 μL of 6×10^{-4} M aqueous solution of a RE nitrate solution is deposited, and then air-dried (circled in Fig. 1). Prior to a detailed discussion of the method, its capabilities and its assumptions, in Fig. 2 we compare low- B AL data obtained at a temperature $T=0.4$ K for twin mesa samples, each with one mesa respectively bare of ions (Fig. 2(a)) and the other covered with an aqueous nitrate solution of Sm^{3+} , Gd^{3+} or Ho^{3+} and dried (Fig. 2(b)). The magnetoresistance (MR) is presented as $\Delta R(B) = R(B) - R(B=0)$ normalized to $R_0 = R(B=0)$, where R stands for the longitudinal resistance (transport coefficient R_{xx}). Measurements occur by standard four-contact low-frequency lock-in techniques. Clear AL phenomena occur as evidenced by a sharp positive MR for $B \sim 0$, crossing over to negative MR at higher B . Clearly also, the AL data in Figs. 2(a) and (b) differ, demonstrating the sensitivity of AL to surface species. The twin mesas are part of the same sample, experience the same processing apart from RE solution coverage, and experience the same cooldown to the experiment T ($0.4 \text{ K} \leq T \leq 5 \text{ K}$). The AL signals are comparatively measured on the bare and covered twin mesas, and it is from the comparative (rather than absolute) data that conclusions are drawn. The paper discusses the interpretation of the comparative AL data.

The air-dried RE nitrate solutions leave a residual film with defined edges. The film forms a visual indication of the RE species concentration on the InAs surface, and reveals a higher concentration (and thus RE species effective areal density) at the edge of the deposited area. Atomic force microscopy shows no cluster formation, however. Since the signal $\Delta R(B)$ results from an average over the serpentine mesas, we infer that the difference in $\Delta R(B)$ between bare and covered mesas reflects a RE areal density averaged over the covered mesa as well. While the averaging limits a detailed study of the dependence on RE density, the method does allow a comparative understanding of the interaction between surface electrons and the different RE species, as presented below. The average sur-

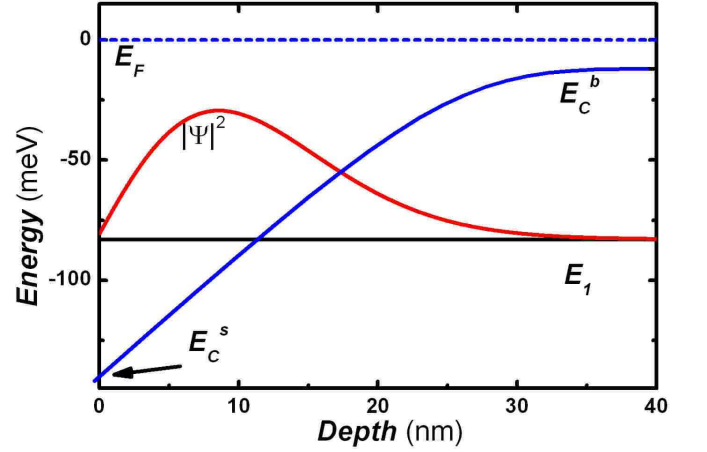


FIG. 4: Schematic band structure at the surface of InAs, where the 2DES has a single occupied subband (the energy levels are explained in the text, and $|\Psi|^2$ represents the probability density (in arbitrary units, with $|\Psi|^2=0$ taken at the E_1 line).

face RE ion density is estimated at $n_{RE} \approx 10^6/\mu\text{m}^2$. The solutions are prepared by dissolving $\text{RE}(\text{NO}_3)_3 \cdot n\text{H}_2\text{O}$ (where $n = 5$ for Gd and Ho, and 6 for Sm) in deionized water, and the starting nitrate solutions have the RE ions in their +3 oxidation states, a relatively stable state¹⁷. Given the low concentration of the solutions (6×10^{-4} M) and complete miscibility of the nitrate salts, a RE nitrate is appreciably hydrated, reducing the probability that RE ions will approach each other, interact and bond or hybridize with the substrate. Contributions to the AL signal from the fabrication process, exposure to deionized water, as well as from the nitrate ions were evaluated. The twin serpentine patterns are fabricated simultaneously, with a deionized water rinse as the final mesa fabrication step. Thus, bare and RE solution covered mesas experience the same environments and are both exposed to deionized water. Further, a control sample with one bare mesa and one covered by deionized water, and subsequently air-dried, was characterized, and no difference in the AL signal was observed. To assess the contributions of the nitrate ions, a Bi^{+3} nitrate solution of the same concentration as the RE solutions was used. Bi^{+3} ions have a spin angular momentum quantum number $S=0$, and thus any comparative changes in the AL data measured between the Bi ion covered versus bare mesa may be attributed to the presence of nitrate ions (data not shown). We do not observe any significant differences in the AL data in these controls, and hence our measurements probe the interactions between the RE ions and InAs surface electrons.

The transverse (R_{xy} , Hall) and longitudinal ($R_{xx} = R$) transport coefficients in Figs. 3(a) and (b) indicate the presence of two carrier types with different carrier density n and mobility μ . By applying a two-carrier fit, we assign one type to the surface accumulation layer electrons with (e.g. in Fig. 3) surface density $n_s = 0.59 \times 10^{12} \text{ cm}^{-2}$ and surface mobility $\mu_s = 22000 \text{ cm}^2/\text{Vs}$, and the other to the bulk electrons with bulk density $n_b = 2.3 \times 10^{16} \text{ cm}^{-3}$ and bulk mobility $\mu_b = 4100 \text{ cm}^2/\text{Vs}$. Table I shows the transport properties for the samples discussed here, including the diffusion

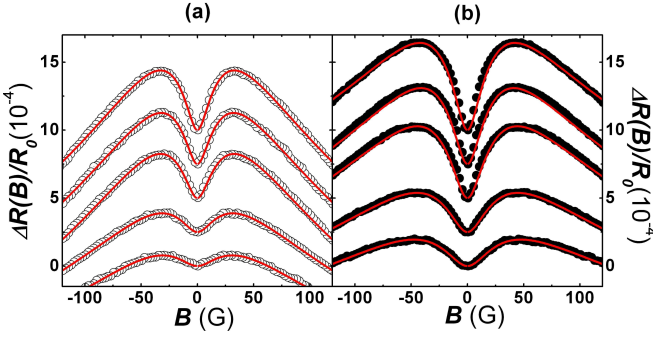


FIG. 5: (a) Magnetoresistance due to AL on bare mesa and (b) on covered mesa, both of the Ho^{3+} sample at (from top to bottom) $T=0.4, 0.7, 1.3, 3.0$ and 5.0 K (1 out of 6 experimental points are plotted, curves offset by 2.5×10^{-4}). Solid lines are theoretical fits.

coefficients D for the surface electrons. For a given sample, mobilities and densities do not vary in the range of the experimental temperatures. Mobilities and densities vary per sample, yet no significantly systematic variation caused by solution coverage is observed. The values of n_s are consistent with previous studies^{14,15}. The assignment is confirmed by a self-consistent calculation, using non-parabolicity in the InAs dispersion, with a Γ -point effective mass of 0.024 and low T band gap of 418 meV. Figure 4 depicts a schematic band struc-

ture and the probability density ($|\Psi|^2$) associated with the surface electron wave function. From n_b , the Fermi level E_F is calculated at 12 meV above E_C^b , the location of the bulk conduction band. We calculate a downward band bending of 130 meV toward the surface¹⁵, pinning the conduction band at E_C^s at the surface. The trace E_C^s to E_C^b in Fig. 4 forms a triangular quantum well close to the surface. Within the triangular quantum well approximation, use of n_s locates the 1st subband energy E_1 at 83 meV below E_F . The 2nd subband energy would then fall above E_F , indicating a single subband system, consistent with the two-carrier fit. The approximate width of the triangular well is calculated at 25 nm and for all samples the Fermi wavelength is about 30 nm. The two-carrier fit is performed for each individual mesa and n_s and μ_s determined, as summarized in Table I.

Figures 2 and 5 show $\Delta R(B)/R_0$, where $R(B)$ was symmetrized to remove components resulting from residual R_{xy} or other slight electronic shifts, and where the parabolic background due to the classical two-carrier MR was subtracted (Fig. 3(b)). In the absence of spin-flip scattering, the quantum corrections to the two-dimensional conductivity $\sigma_2(B)$ arising from AL are sensitive to τ_0 , τ_i and τ_{SO} . In the presence of spin-flip scattering, τ_i is to be replaced by the phase coherence time τ_ϕ ^{18,19} defined as $\tau_\phi^{-1} = \tau_i^{-1} + 2\tau_s^{-1}$, and τ_{SO}^{-1} by $(\tau_{SO}^{-1} - \tau_s^{-1})$ ¹⁹. An expression for $\Delta\sigma_2(B) = \sigma_2(B) - \sigma_2(B=0)$ is then obtained as^{9,20}:

$$\Delta\sigma_2(B) = \frac{e^2}{2\pi^2\hbar} \left\{ - \left[\psi\left(\frac{1}{2} + \frac{B_0}{B}\right) - \psi\left(\frac{1}{2} + \frac{B_i + B_{SO} + B_s}{B}\right) + \frac{1}{2}\psi\left(\frac{1}{2} + \frac{B_i + 2B_s}{B}\right) - \frac{1}{2}\psi\left(\frac{1}{2} + \frac{B_i + 2B_{SO}}{B}\right) \right] + \left[\ln\left(\frac{B_0}{B}\right) - \ln\left(\frac{B_i + B_{SO} + B_s}{B}\right) + \frac{1}{2}\ln\left(\frac{B_i + 2B_s}{B}\right) - \frac{1}{2}\ln\left(\frac{B_i + 2B_{SO}}{B}\right) \right] \right\} \quad (1)$$

where $\psi(x)$ is the digamma function and each scattering time τ_α (with $\alpha = 0, i, SO, s$) corresponds to a characteristic magnetic field $B_\alpha = \hbar/(4eD\tau_\alpha)$. Since $\Delta R(B) \ll R_0$ we linearize to $\Delta\sigma_2(B)/\sigma_2(B=0) \approx -\Delta R(B)/R_0$ which allows direct comparison to experimental $R(B)$ values. Experimentally, our data follow Eq. (1) to good precision.

B_i , B_{SO} and B_s are fitting parameters allowing the determination of τ_i , τ_{SO} and τ_s , while B_0 is independently and separately known from τ_0 for all mesas. We notice that in Eq. (1) the terms with B_i , B_{SO} and B_s can be expressed in 2 combinations, namely $B_i + 2B_s$ corresponding to $B_\phi = \hbar/(4eD\tau_\phi)$, and $B_{SO} - B_s$. As a result, only 2 of 3 unknown parameters can be independently determined from one data set. Two data sets, on twin bare and solution-covered mesas, are necessary to determine B_i , B_{SO} and B_s ¹. On the bare mesas, no intentional magnetic impurities are introduced, and we assume $B_s \rightarrow 0$, resulting in $B_\phi \rightarrow B_i$ and $B_{SO} - B_s \rightarrow B_{SO}$. For the bare mesas B_i and B_{SO} can then be determined from the data. From experiments on metal systems¹ it is known that magnetic impurities introduce spin-flip scattering and ad-

ditional spin-orbit scattering, but do not affect inelastic scattering. Thus τ_i can be assumed the same for bare and covered twin mesas fabricated on the same sample. Then this τ_i yields a value for B_i for the corresponding covered mesa by using $B_i = \hbar/4eD\tau_i$ with D as measured in the covered mesa (from Table I). Next B_{SO} and B_s are determined for the covered mesa by fitting Eq. (1). By this method τ_i , τ_{SO} and τ_s are obtained for the covered mesas and τ_i and τ_{SO} ($\tau_s \rightarrow \infty$) for the bare mesas.

Figure 5 uses the Ho^{3+} sample as example to show the correspondence between data and theoretical fit for both bare and covered mesas at different T . A 5% variation in τ_i , τ_{SO} and τ_s can be applied to the values obtained from the fits and still obtain a good correspondence with the data, and 5% error bars are thus applied to the remainder of the work. Different fitting models apart from Eq. (1) also lead to different values, varying by up to 30%. However, it is important to note that the relative values of τ_i , τ_{SO} and τ_s , between bare and solution-covered twin mesas, and between different T values, do not vary significantly if the same model is applied con-

TABLE I: Surface accumulation layer electron transport properties: n_s , μ_s , and D , at $T=0.4$ K.

| | Covered mesa (Ho ³⁺) | Bare mesa (Ho ³⁺) | Covered mesa (Sm ³⁺) | Bare mesa (Sm ³⁺) | Covered mesa (Gd ³⁺) | Bare mesa (Gd ³⁺) |
|---------------------------------------|-------------------------------------|----------------------------------|-------------------------------------|----------------------------------|-------------------------------------|----------------------------------|
| n_s (10^{12} cm ⁻²) | 0.61 | 0.55 | 0.63 | 0.59 | 0.61 | 0.69 |
| μ_s (10^4 cm ² /Vs) | 2.4 | 2.1 | 2.5 | 2.2 | 3.0 | 2.1 |
| D (10^3 cm ² /s) | 1.2 | 0.9 | 1.2 | 1.0 | 1.5 | 1.1 |

sistently. Likewise, the uncertainty in transport parameters (such as D), will not affect the relative values of τ_i , τ_{SO} and τ_s either. Hence reliable information can be drawn from the comparative trends related to the RE ion and under varying T , although absolute values for the scattering times cannot be quoted to better than 30%. Figures 6 and 7 contain the experimental results, presented as scattering rates as function of T (with associated error bars). The modification of the scattering rates due to the presence of the RE ions is assigned predominantly to the single-subband surface electrons and not to the bulk electrons, since the proximity of the surface electrons to the surface local moments enhances the interactions. The AL analysis also proceeds under the approximation that we may neglect the AL contribution from the bulk layer without introducing substantial distortion of the results. This approximation rests on the fact that SOI in the bulk is small compared to the strong Rashba SOI at the surface, and hence the bulk contribution to the AL signal is expected to be smaller than the surface contribution. Moreover, the twin-mesa comparative approach (bare vs covered mesas) emphasizes the difference in AL signal due to RE ion coverage, a difference likely to be dominated by the surface contribution. In the AL analysis we have also neglected the electron-electron scattering between surface and bulk electrons, because an upper bound for the electron-electron scattering rate τ_{ee}^{-1} can be estimated¹¹ to lie in the range $0.3 \times 10^{10} \text{ s}^{-1} < \tau_{ee}^{-1} < 5 \times 10^{10} \text{ s}^{-1}$ for $0.4 \text{ K} \leq T \leq 5 \text{ K}$. The rate τ_{ee}^{-1} is thus expected to be about an order of magnitude slower than the other scattering rates, $10^{11} \text{ s}^{-1} < \tau_\alpha^{-1} < 10^{12} \text{ s}^{-1}$ ($\alpha = i, SO, s$), and neglect of electron-electron scattering, especially between spatially separated surface and bulk electrons, is justified.

Figure 6 shows the T dependence of τ_i^{-1} , adopted as common for both bare and RE ion-covered mesas. The linear dependence $\tau_i^{-1} \sim T$ is consistent with dominant Nyquist decoherence²³ arising from fluctuations in the electromagnetic background. The spin-orbit scattering rate τ_{SO}^{-1} increases in the presence of RE ions, as comparison in Fig. 6 demonstrates. SOI is influenced by atomic weight, and Fig. 6 demonstrates that heavy elements such as the REs can increase the average SOI experienced by carriers in their proximity, leading to the observed experimental result. The increase by adatom coverage has been observed in metals systems⁷ and has been proposed as a means of increasing the average SOI in low-SOI systems like graphene²¹. Figure 6 indicates that for both bare and covered mesas τ_{SO}^{-1} is not strongly T -dependent within the experiment range of T , consistent with previous

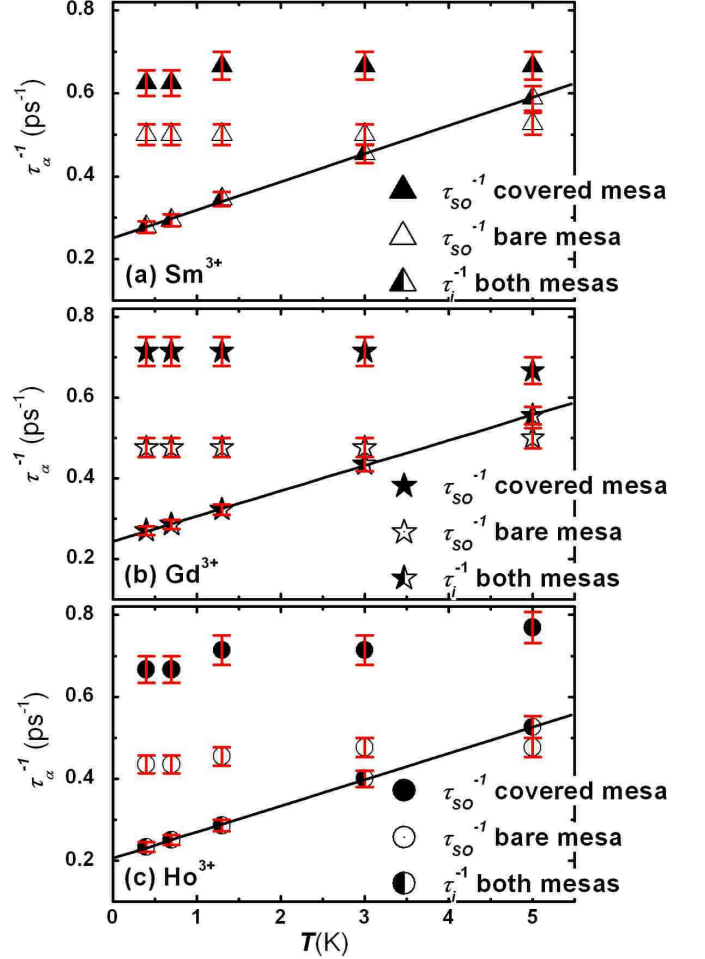


FIG. 6: Different scattering rates τ_α^{-1} ($\alpha = SO$ or i) vs T for (a) Sm³⁺ (triangles) sample; (b) Gd³⁺ (stars) sample; (c) Ho³⁺ (circles) sample. In all the graphs solid symbols stand for τ_{SO}^{-1} of the ion-covered mesa; open symbols stand for τ_{SO}^{-1} of the bare mesa; half-solid symbols stand for τ_i^{-1} of both mesas, sharing the same value. Solid lines form guides to the eye. Error bars are indicated.

discussions²². The residual T -dependence, and the small differences in relative magnitudes of the increase in τ_{SO}^{-1} dependent on RE ion, are the result of several competing effects and must be relegated to future study.

Figure 7 indicates that the spin-flip rate τ_s^{-1} is strongly influenced by the type of RE ion deposited. A magnetic inter-

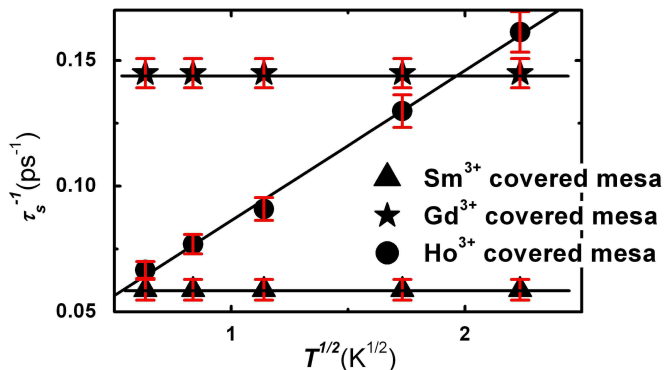


FIG. 7: The spin-flip rate τ_s^{-1} of ion-covered mesas vs $T^{1/2}$. Solid lines form guides to the eye. Error bars are indicated.

action $\sigma \cdot \mathbf{S}$ between local RE moments \mathbf{S} and electron spins σ hence exists, where \mathbf{S} denotes the total spin of the RE ion 4f electrons. The presence of the interaction is borne out in Fig. 7 by the influence of the ions on τ_s^{-1} , showing a modification of the electron spin states in the presence of the RE ions. Sm^{3+} , Gd^{3+} , and Ho^{3+} differ in the magnitude of the spin-flip rate they impart, as well as its dependence on T , properties which will be discussed below. Free from a substrate the RE ions are characterized by paramagnetic behavior with effective magnetic moments due to partially filled 4f shells. The effective moments μ_{eff} are expressed in Bohr magnetons (μ_B), with Sm^{3+} having $\mu_{eff} = 1.5\mu_B$, Gd^{3+} having $\mu_{eff} = 8.0\mu_B$, and Ho^{3+} having $\mu_{eff} = 10.4\mu_B$. The spin S , orbital L and total angular momentum quantum numbers J of the RE ions in their ground state are as follows, following Hund's rules: Sm^{3+} has $S=\frac{5}{2}$, $L=5$ and $J=\frac{5}{2}$; Gd^{3+} has $S=\frac{7}{2}$, $L=0$ and $J=\frac{7}{2}$; Ho^{3+} has $S=2$, $L=6$ and $J=8$. One may expect paramagnetic behavior to be maintained on a substrate, since the 4f shells are partially shielded by the outermost s and p shells and crystal field effects will hence be small. However, the magnetic moments of the RE ions may still be locked to specific orientations by interaction with the substrate atoms, or by Rudermann-Kittel-Kasuya-Yosida (RKKY) interactions^{3,24,25}, leading to spin-glass behavior. Both a paramagnetic system or a spin-glass lead to spin-flip scattering. To identify which of the two is occurring on the InAs surface, we have to ascertain how respectively paramagnetic behavior and T -dependent spin-glass formation influence τ_s^{-1} . Spin-glasses can occur with the axes of the moments distributed isotropically (Heisenberg spin-glass), or aligned parallel or antiparallel (Ising spin-glass). Under the present case of strong spin-orbit scattering ($\tau_{SO}^{-1} \gtrsim \tau_i^{-1}$) however, both spin-glasses are predicted to lead to the same reduction in τ_s^{-1} by $S/(S+1)$ compared to the free-spin case^{24,26}.

For Sm^{3+} and Gd^{3+} Fig. 7 shows a τ_s^{-1} independent of T . The higher spin-flip rate observed for Gd^{3+} correlates with its higher moment ($8.0\mu_B$, compared to $1.5\mu_B$ for Sm^{3+}). For Sm^{3+} and Gd^{3+} we observe no T -dependence in the data, and hence no conclusion can be drawn about spin-glass behavior. For Ho^{3+} Fig. 7 shows a dependence $\tau_s^{-1} \sim T^n$ with $n \approx \frac{1}{2}$. We note that *paramagnetic* alignment due to

the B applied normal to the sample is expected to be negligible. The fraction of the RE ions aligned along the applied B can be calculated as $f = gJ\mu_B B_J(x)/\mu_{eff}$, with $x = gJ\mu_B B/(k_B T)$, and with g the Landé factor, $B_J(x)$ the Brillouin function and k_B the Boltzmann constant. In the experimental range analyzed for AL, B/T reaches 300 G/K, at $T=0.4$ K and $B=120$ G. A maximal paramagnetic alignment f of 0.32% is then expected for Sm^{3+} , 5.2% for Gd^{3+} , and 7.2% for Ho^{3+} . The effect of the alignment on the average spin-flip rate can be calculated by considering the fraction f of aligned spins and multiplying the rate by $S/(S+1)$ for this fraction. From this calculation, when lowering T from 5 K to 0.4 K paramagnetic alignment is expected to reduce τ_s^{-1} by a factor of 0.999 for Sm^{3+} , of 0.988 for Gd^{3+} , and of 0.976 for Ho^{3+} . The relative reduction in τ_s^{-1} due to any paramagnetic alignment during the experiment is thus small, and below the measurement threshold for all RE ions. Moreover, for Ho^{3+} , a complete alignment due to spin-glass formation at $T = 0.4$ K starting from a free-spin case at $T = 5$ K would lead reduction of τ_s^{-1} by a factor $S/(S+1) = \frac{2}{3}$ on cooling from 5 K to 0.4 K. Yet, the experimentally determined ratio of the spin-flip rates at 0.4 K ($\tau_s^{-1} = 0.067$ ps⁻¹) and at $T = 5$ K ($\tau_s^{-1} = 0.16$ ps⁻¹) is 0.42, a stronger reduction than the maximal spin-glass case can account for. Hence, whereas no conclusion can be drawn about spin-glass formation for Sm^{3+} and Gd^{3+} , for Ho^{3+} spin-glass formation is unlikely to lie at the origin of our observations.

The dependence $\tau_s^{-1} \sim T^{\frac{1}{2}}$ we observe for InAs electrons interacting with Ho^{3+} , was also observed in Kondo systems below their Kondo temperature (T_K), formed between itinerant electrons and local impurity moments^{5,26}. At low T a single Kondo impurity forms a spin-singlet state with surrounding electrons within a Kondo cloud. Below T_K the moment of the magnetic Kondo impurity is screened by the electrons, and spin-flip scattering is then increasingly suppressed as T is lowered below T_K , while reaching a maximum at T_K ^{1,6,18,33,34}. The present experiments are limited to $T < 5$ K due to the requirement of quantum coherence for the AL signal. However, from the monotonous decrease in τ_s^{-1} with decreasing T we deduce that if Kondo physics is indeed active, then the data indicate $T_K > 5$ K. However, in our n -InAs system the low electron density and comparatively dense ion coverage, the high spin from the underscreened RE ions, and the strong SOI exclude such a high $T_K > 5$ K. The observed T dependence of τ_s^{-1} in the Ho^{3+} case can thus not be explained by the formation of a Kondo system.

An origin for the $\tau_s^{-1} \sim T^{\frac{1}{2}}$ observed for InAs electrons interacting with Ho^{3+} may lie in the large number of low-lying energy levels generated by the incompletely filled 4f levels of RE ions, leading to characteristically dense energy spectra. For triply ionized RE ions, crystal field effects typically do not lead to a major rearrangement of energy levels²⁷, and relevant energy levels can thus approximately be identified from Ho^{3+} spectra in various solid-state environments. The existence of spin-flips in the electron system implies a change in \mathbf{S} for the RE ion. We thus want to identify transitions from the 5I_8 ground state of Ho^{3+} to states of different S , within $k_B T \approx 0.5$ meV from the ground state at our measurement

temperatures. The 4f electrons in RE ions form multiplets arising from SOI following the Russell-Saunders approximation, with splitting between multiplet levels of $\lambda \mathbf{L} \cdot \mathbf{S}$, where λ is the SOI constant for particular L and S in the RE ion. The multiplet levels are characterized by a J value with $2S+1$ possible values. The energy difference between the ground state 5I_8 and the next multiplet member, 5I_7 , is however 626 meV²⁸ \gg 0.5 meV, and 5I_8 and 5I_7 share the same $S=2$ value. The excited multiplet 3K_8 state of Ho^{3+} however, situated 5.1 meV above 5I_8 , can answer the criteria for thermally excited spin-flip transitions, especially if the levels are further split or broadened due to proximity to the InAs surface. In previous work^{30,31} it has been noted that the ground state 5I_8 has substantial admixture of 3K_8 states, reinforcing the possibility of transitions mediated by InAs surface electrons, with accompanying spin-flip. We note that, compared to Ho^{3+} , Sm^{3+} has a low $\mu_{eff} = 1.5\mu_B$ which will reduce the spin-flip rate, while Gd^{3+} has $L=0$, suppressing the splitting due to $\lambda \mathbf{L} \cdot \mathbf{S}$, and hence has a spectrum characterized by a large (≈ 4 eV) gap between its $^8S_{7/2}$ ground state and the next excited state. Apart from multiplet level splittings, Ho^{3+} is susceptible to other mechanisms leading to finer level structure. From the lifetime of resonance levels, it is known that coupling between crystal electric fields and the hydrated salts of the outlying lanthanide ions such as Ho^{3+} , is higher than for mid-series lanthanide ions (here particularly Gd^{3+} but also Sm^{3+})^{27,29}. The higher coupling to the environment for Ho^{3+} may lead to an electric Stark splitting of levels into $2J+1$ closely spaced levels, with a spacing sensitively dependent on the magnitude and symmetry of the environmental electric field. Hyperfine splitting

should also be considered^{27,30-32}, particularly again for Ho^{3+} due to the large value for its nuclear magnetic moment (in nuclear magnetons: 4.01 for Ho, compared to -0.21 for Sm and -0.11 for Gd averaged over their isotopes). A splitting of ~ 1.5 meV has been quoted³⁰, in range for thermal excitations in the present experiments although the precise value will depend on environmental factors. An exact quantitative assessment of the transitions responsible for our experimental observation that $\tau_s^{-1} \sim T^{1/2}$ for electrons interacting with Ho^{3+} cannot presently be deduced from the data. It is significant however that the AL measurement of τ_s^{-1} identifies a pronounced T dependence for Ho^{3+} , and a higher spin-flip rate for Gd^{3+} than for Sm^{3+} , as these results are indeed borne out from their magnetic moments and energy level spectra.

In conclusion, using antilocalization measurements we observe spin interactions between two-dimensional electrons at the surface of InAs and local moments from rare earth ions Sm^{3+} , Gd^{3+} , and Ho^{3+} deposited on the surface. The measurements provide the magnitude and temperature dependence of the spin-flip rate, the spin-orbit scattering rate, and the inelastic scattering rate of the InAs surface electrons as modified by the rare earth ions. The experiments show that the strength of the spin-orbit interaction can be modified by the proximity of rare earth ions. We also demonstrate an accordance between the modified surface electron spin-flip rates and the rare earth ion energy level structures and magnetic moments. The authors thank K. Park and T. Dietl for useful discussions. This work was supported by the DOE through Grant No. DOE DE-FG02-08ER46532.

* Electronic address: heremans@vt.edu; Author to whom correspondence should be addressed: Department of Physics, Virginia Tech, Blacksburg, VA 24061, USA

¹ W. Wei, and G. Bergmann, Phys. Rev. B **37**, 5990 (1988).

² J.J. Zhu, D.X. Yao, S.C. Zhang, and K. Chang, Phys. Rev. Lett. **106**, 097201 (2011); P. Wahl, P. Simon, L. Diekhöner, V.S. Stepanyuk, P. Bruno, M.A. Schneider, and K. Kern, Phys. Rev. Lett. **98**, 056601 (2007).

³ L. Zhou, J. Wiebe, S. Lounis, E. Vedmedenko, F. Meier, S. Blügel, P.H. Dederichs, and R. Wiesendanger, Nat. Phys. **6**, 187 (2010).

⁴ T. Gang, M. Deniz Yilmaz, D. Atac, S. K. Bose, E. Strambini, A. H. Velders, M. P. de Jong, J. Huskens, and W. G. van der Wiel, Nat. Nanotechnol. **7**, 232 (2012).

⁵ R. Schäfer, and G. Bergmann, Solid State Comm. **98**, 45 (1996).

⁶ F. Mallet, J. Ericsson, D. Mailly, S. Ünlübayir, D. Reuter, A. Melnikov, A.D. Wieck, T. Micklitz, A. Rosch, T.A. Costi, L. Saminadayar, and C. Bäuerle, Phys. Rev. Lett. **97**, 226804 (2006).

⁷ G. Bergmann, Phys. Rep. **107**, 1 (1984).

⁸ S. McPhail, C.E. Yasin, A.R. Hamilton, M.Y. Simmons, E.H. Linfield, M. Pepper, and D.A. Ritchie, Phys. Rev. B **70**, 245311 (2004).

⁹ S. Hikami, A.I. Larkin, and Y. Nagaoka, Prog. Theor. Phys. **63**, 707 (1980).

¹⁰ M. Kohda, T. Bergsten, and J. Nitta, J. Phys. Soc. Jpn. **77**, 031008 (2008).

¹¹ J. J. Lin, and J. P. Bird, J. Phys.: Condens. Matter **14**, R501

(2002).

¹² D.C. Tsui, Phys. Rev. B **12**, 5739 (1975).

¹³ T. Mochizuki, R. Masutomi, and T. Okamoto, Phys. Rev. Lett. **101**, 267204 (2008).

¹⁴ M. Noguchi, K. Hirakawa, and T. Ikoma, Phys. Rev. Lett. **66**, 2243 (1991).

¹⁵ L.F.J. Piper, T.D. Veal, M.J. Lowe, and C.F. McConville, Phys. Rev. B **73**, 195321 (2006).

¹⁶ C. Schierholz, T. Matsuyama, U. Merkt, and G. Meier, Phys. Rev. B **70**, 233311 (2004).

¹⁷ B. G. Wybourne, *Spectroscopic Properties of Rare Earths*, (Interscience Publishers, New York, 1965).

¹⁸ C. Van Haesendonck, J. Vranken, and Y. Bruynseraede, Phys. Rev. Lett. **58**, 1968 (1987).

¹⁹ J.C. Licini, G.J. Dolan, and D.J. Bishop, Phys. Rev. Lett. **54**, 1585 (1985).

²⁰ S.V. Iordanskii, Yu.B. Lyanda-Geller, and G.E. Pikus, JETP Lett. **60**, 206 (1994).

²¹ C. Weeks, Jun Hu, J. Alicea, M. Franz, and R. Wu, Phys. Rev. X **1**, 021001 (2011).

²² R.L. Kallaher, and J.J. Heremans, Phys. Rev. B **79**, 075322 (2009).

²³ B.L. Altshuler, A.G. Aronov, and D.E. Khmel'nitsky, J. Phys. C: Solid State Phys. **15**, 7367 (1982).

²⁴ W. Wei, G. Bergmann, and R.-P. Peters, Phys. Rev. B **38**, 11751 (1988).

- ²⁵ M.A. Ruderman, and C. Kittel, Phys. Rev. **96**, 99 (1954).
- ²⁶ R.P. Peters, G. Bergmann, and R. M. Mueller, Phys. Rev. Lett. **60**, 1093 (1988).
- ²⁷ G. H. Dieke, and H. M. Crosswhite, Applied Optics **2**, 675 (1963).
- ²⁸ B. R. Judd, Proc. Phys. Soc. (London) **69**, 157 (1956).
- ²⁹ G. H. Dieke, and L. A. Hall, J. Chem. Phys. **27**, 465 (1957).
- ³⁰ B. G. Wybourne, J. Chem. Phys. **37**, 1807 (1962).
- ³¹ D. St. P. Bunbury, C. Carboni, and M. A. H. McCausland, J. Phys.:Condens. Matter **1**, 1309 (1989).
- ³² J. Pelzl, S. Hüfner, and S. Scheller, Z. Physik **231**, 377 (1970).
- ³³ R.P. Peters, G. Bergmann, and R. M. Mueller, Phys. Rev. Lett. **58**, 1964 (1987).
- ³⁴ G.M. Alzoubi, and N.O. Birge, Phys. Rev. Lett. **97**, 226803 (2006).
- ³⁵ T. Micklitz, A. Altland, T.A. Costi, and A. Rosch, Phys. Rev. Lett. **96**, 226601 (2006).
- ³⁶ G. Zaránd, L. Borda, J. von Delft, and N. Andrei, Phys. Rev. Lett. **93**, 107204 (2004).
- ³⁷ C. Bäuerle, F. Mallet, F. Schopfer, D. Mailly, G. Eska, and L. Saminadayar, Phys. Rev. Lett. **95**, 266805 (2005).
- ³⁸ Y. Meir, N.S. Wingreen, Phys. Rev. B **50**, 4947 (1994).